nature chemistry

ARTICLES

https://doi.org/10.1038/s41557-022-01039-3

Check for updates

Synthesis and single-molecule imaging reveal stereospecific enhancement of binding kinetics by the antitumour eEF1A antagonist SR-A3

Hao-Yuan Wang[1], Haojun Yang[2,6], Mikael Holm[3,6], Harrison Tom[2], Keely Oltion[1], Amjad Ayad Qatran Al-Khdhairawi[4], Jean-Frédéric F. Weber[5], Scott C. Blanchard[3], Davide Ruggero[1,2] and Jack Taunton[1]✉

Ternatin-family cyclic peptides inhibit protein synthesis by targeting the eukaryotic elongation factor-1α. A potentially related cytotoxic natural product ('A3') was isolated from *Aspergillus*, but only 4 of its 11 stereocentres could be assigned. Here, we synthesized SR-A3 and SS-A3—two out of 128 possible A3 epimers—and discovered that synthetic SR-A3 is indistinguishable from naturally derived A3. Relative to SS-A3, SR-A3 exhibits an enhanced residence time and rebinding kinetics, as revealed by single-molecule fluorescence imaging of elongation reactions catalysed by eukaryotic elongation factor-1α in vitro. An increased residence time—stereospecifically conferred by the unique β-hydroxyl in SR-A3—was also observed in cells. Consistent with its prolonged duration of action, thrice-weekly dosing with SR-A3 led to a reduced tumour burden and increased survival in an aggressive Myc-driven mouse lymphoma model. Our results demonstrate the potential of SR-A3 as a cancer therapeutic and exemplify an evolutionary mechanism for enhancing cyclic peptide binding kinetics via stereospecific side-chain hydroxylation.

All living organisms rely on protein synthesis mediated by the ribosome and its associated translation factors. Bacterial ribosomes have long been targeted by small-molecule antimicrobials[1], while the human ribosome and translation factors have recently emerged as promising drug targets for cancer and viral infections[2,3]. Eukaryotic elongation factor-1α (eEF1A) is an essential component of the translation machinery[4]. GTP-bound eEF1A delivers aminoacyl-transfer RNAs (aa-tRNAs) to the ribosomal A site during the elongation phase of protein synthesis. Base pairing between the A-site messenger RNA (mRNA) codon and the aa-tRNA anticodon promotes GTP hydrolysis by eEF1A, releasing the aa-tRNA from eEF1A and allowing its accommodation into the ribosome. The growing protein chain is subsequently transferred from the P-site peptidyl tRNA to the A-site aa-tRNA, extending it by one amino acid through ribosome-catalysed peptide bond formation.

Tumour cells and viruses hijack the protein synthesis machinery to elicit growth and replication. Specific eEF1A inhibitors—all of which are macrocyclic natural products—have been evaluated as potential anticancer and antiviral drugs[5]. Didemnin B[6,7], cytotrienin A[8], nannocystin A[9] and cordyheptapeptide A[10] are examples of structurally diverse macrocycles that bind eEF1A and inhibit translation elongation. Dehydro-didemnin B (plitidepsin) is approved in Australia for the treatment of relapsed/refractory multiple myeloma[11] and is efficacious in SARS-CoV-2 infection models[12].

The cyclic heptapeptide A3 was isolated from an *Aspergillus* strain on the basis of its ability to inhibit cancer cell proliferation at low nanomolar concentrations[13]. Although the amino acid composition, sequence and *N*-methylation pattern of A3 were deduced, only four out of 11 stereocentres could be assigned (Fig. 1). Motivated by its potent anti-proliferative activity and unknown mechanism of action, we sought to determine which of the 128 possible stereoisomers (based on seven unassigned stereocentres) corresponds to A3. Based on our observation that the amino acid sequence and *N*-methylation pattern of A3 and ternatin are similar[14], we had previously designed and synthesized ternatin-4, which incorporates the dehydromethyl leucine (dhML) and pipecolic acid residues found in A3, yet lacks the β-hydroxy group attached to *N*-Me-Leu (Fig. 1). We discovered that ternatin-4 inhibits cancer cell proliferation and SARS-CoV-2 replication by targeting eEF1A[15,16]. However, the precise step(s) of eEF1A-catalysed elongation blocked by ternatin-family cyclic peptides—as well as the structure of A3 and the role of its unique β-hydroxy group—all remained unknown.

Here, we report the total syntheses of two A3 epimers, SR-A3 and SS-A3 (Fig. 1), along with cellular and single-molecule biophysical studies focused on quantifying drug-target residence times. Synthetic SR-A3 potently inhibited cell proliferation and protein synthesis by targeting eEF1A and was spectroscopically and biologically indistinguishable from the natural product A3. Transient exposure of cells to SR-A3 resulted in long-lasting inhibitory effects, whereas similarly prolonged effects were not observed with SS-A3 or ternatin-4. To gain mechanistic insight into these differences, we assessed eEF1A-catalysed translation via single-molecule fluorescence resonance energy transfer (smFRET) imaging. These experiments directly revealed SR-A3's comparatively long duration of eEF1A blockade on the ribosome, enabled in part by its enhanced capacity to rebind following dissociation. Preclinical studies in a mouse model of human Burkitt lymphoma revealed that SR-A3, but

[1]Department of Cellular and Molecular Pharmacology, University of California, San Francisco, CA, USA. [2]Department of Urology, University of California, San Francisco, CA, USA. [3]Department of Structural Biology, St. Jude Children's Research Hospital, Memphis, TN, USA. [4]School of Pharmacy, Faculty of Health & Medical Sciences, Taylor's University Lakeside Campus, Subang Jaya, Malaysia. [5]Atta-ur-Rahman Institute for Natural Product Discovery (AuRIns), Universiti Teknologi MARA (UiTM) Selangor Branch, Bandar Puncak Alam, Malaysia. [6]These authors contributed equally: Haojun Yang, Mikael Holm. ✉e-mail: jack.taunton@ucsf.edu

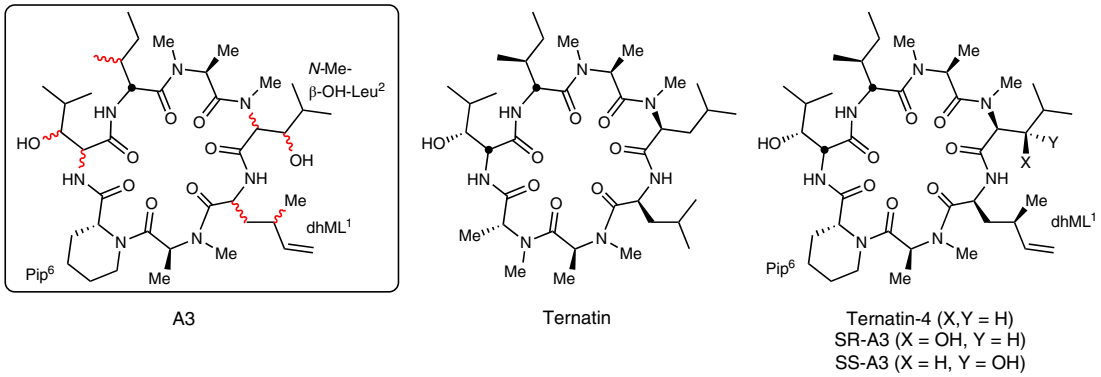

Fig. 1 | Partially determined structure of the natural product A3. We hypothesized that A3 corresponds to one of two epimers—SR-A3 or SS-A3—related to ternatin, a natural product, and ternatin-4, an A3-inspired synthetic compound[14]. Pip, pipecolic acid.

not ternatin-4, exhibits potent antitumour activity. Our data thus reveal a striking and stereospecific enhancement in eEF1A binding kinetics conferred by a single oxygen atom appended to a cyclic peptide.

Results

Synthesis of SR-A3 and SS-A3 via an expeditious route to dhML. We speculated that dhML in the natural product A3 has the same stereochemistry as in the synthetic compound, ternatin-4 (Fig. 1). Because our original six-step synthesis of dhML methyl ester was low yielding and required a costly chiral auxiliary, we developed a more efficient, second-generation synthesis suitable for preparing gram quantities of Fmoc-dhML (Fmoc, the fluorenylmethoxycarbonyl protecting group).

Copper(I)-promoted S_N2' reaction of a serine-derived organozinc reagent with allylic electrophiles has been previously used to synthesize amino acids that contain a γ-stereogenic centre[17,18]. This method was appealing because it would provide dhML (as the tert-butoxycarbony (Boc) methyl ester) in only two steps from the inexpensive chiral building block, Boc-(*S*)-serine-OMe[17]. After extensive optimization aimed at improving S_N2' versus S_N2 selectivity and conversion (Extended Data Fig. 1), we obtained Boc-dhML-OMe **3** in 43% isolated yield (1.6 g) through the use of 50 mol% CuBr·DMS (DMS, dimethyl sulfide) and two equivalents of crotyl chloride (Fig. 2a). Boc to Fmoc exchange, followed by ester hydrolysis, provided Fmoc-dhML **5**, which was incorporated into the linear heptapeptide as described below.

A solid-phase route was previously employed to synthesize a linear heptapeptide precursor of ternatin, followed by solution-phase cyclization[14]. However, this strategy involved macrocyclization between the secondary amine of *N*-Me-Ala7 and the carboxylic acid of Leu1 (Fig. 2b, site A), which we found to be low yielding in the context of peptides containing dhML[15]. Thus, we sought to identify an alternative cyclization site using the ternatin-related cyclic peptide **6** as a model system (Fig. 2c). Linear heptapeptide precursors were synthesized on the solid phase, deprotected and cleaved from the resin, and cyclized in solution (Supplementary Information for details). Gratifyingly, cyclization at site B provided **6** in 63% overall yield (including the solid-phase linear heptapeptide synthesis), whereas cyclization at site A was less efficient (46% overall yield). By synthesizing the linear heptapeptide precursor on the solid phase and cyclizing in solution at site B, we were able to prepare ternatin-4 in three days and 70% overall yield (27 mg), a substantial improvement over our previous route (Fig. 2c). Most importantly, by incorporating Fmoc-protected (*S*,*R*)- and (*S*,*S*)-*N*-Me-β-OH-Leu, we completed a total syntheses of SR-A3 (21 mg, 35% overall yield) and SS-A3 (5 mg, 21% overall yield).

Synthetic SR-A3 is indistinguishable from naturally derived A3. With synthetic SR-A3 and SS-A3 in hand (Fig. 3a), we first compared their HPLC elution profiles with an authentic sample of the *Aspergillus*-derived natural product A3. SR-A3 and naturally derived A3 had identical retention times, whereas SS-A3 eluted later in the gradient (Fig. 3b). Furthermore, the ^{1}H and ^{13}C NMR spectra of SR-A3 were identical to the corresponding spectra of natural A3 (Fig. 3c). Finally, SR-A3 and naturally derived A3 blocked proliferation of HCT116 cancer cells with superimposable dose–response curves (Fig. 3d; $IC_{50} \approx 0.9$ nM (IC_{50}, half maximal inhibitory concentration)), whereas SS-A3 was about threefold less potent ($IC_{50} \approx 2.7$ nM). Similar trends were observed in four additional cancer cell lines (Extended Data Fig. 2). Together, these data are consistent with our stereochemical hypothesis and strongly suggest that synthetic SR-A3 and natural A3 have the same structure.

***N*-Me-β-OH-Leu stereospecifically confers increased cellular residence time.** We previously demonstrated that ternatin-4 is inactive towards a human cancer cell line that is homozygous for an Ala399Val mutation in eEF1A (encoded by the *EEF1A1* gene)[15]. These cells were also resistant to SR-A3 ($IC_{50} \gg 1$ μM), providing strong genetic evidence that eEF1A is the relevant target (Fig. 4a). Consistent with this interpretation, treatment of cells with SR-A3 for 24 h inhibited global protein synthesis with an IC_{50} of ~20 nM (Fig. 4b), as measured by a clickable puromycin (*O*-propargyl puromycin, OPP) incorporation assay (Extended Data Fig. 3)[19]. Under these conditions—24 h of continuous treatment prior to a 1 h pulse with OPP—SR-A3 behaved identically to ternatin-4, whereas SS-A3 was slightly less potent. Based on these cellular data, it remained unclear as to whether *N*-Me-β-OH-Leu in SR-A3 confers any advantage over the biosynthetically less ornate *N*-Me-Leu found in ternatin and ternatin-4.

Drug-target residence time, which reflects not only the biochemical off-rate, but also the rebinding rate and local target density in vivo, has emerged as a critical kinetic parameter in drug discovery[20,21]. To test for potential differences in cellular residence time, we treated HCT116 cells with 100 nM SR-A3, SS-A3 or ternatin-4 for 4 h, followed by wash-out into drug-free media. At various times post-wash-out, cells were pulse-labelled with OPP for 1 h. Whereas protein synthesis rates partially recovered in cells treated with ternatin-4 or SS-A3 (~30% of dimethyl sulfoxide (DMSO) control levels, 24 h post-wash-out), transient exposure of cells to SR-A3 resulted in more prolonged inhibition (Fig. 4c). To confirm the extended duration of action observed with SR-A3, we assessed cell proliferation during a 72 h wash-out period. Strikingly, cell proliferation over 72 h was sharply reduced after 4 h treatment with 100 nM SR-A3, followed by rigorous wash-out. By contrast, cell proliferation

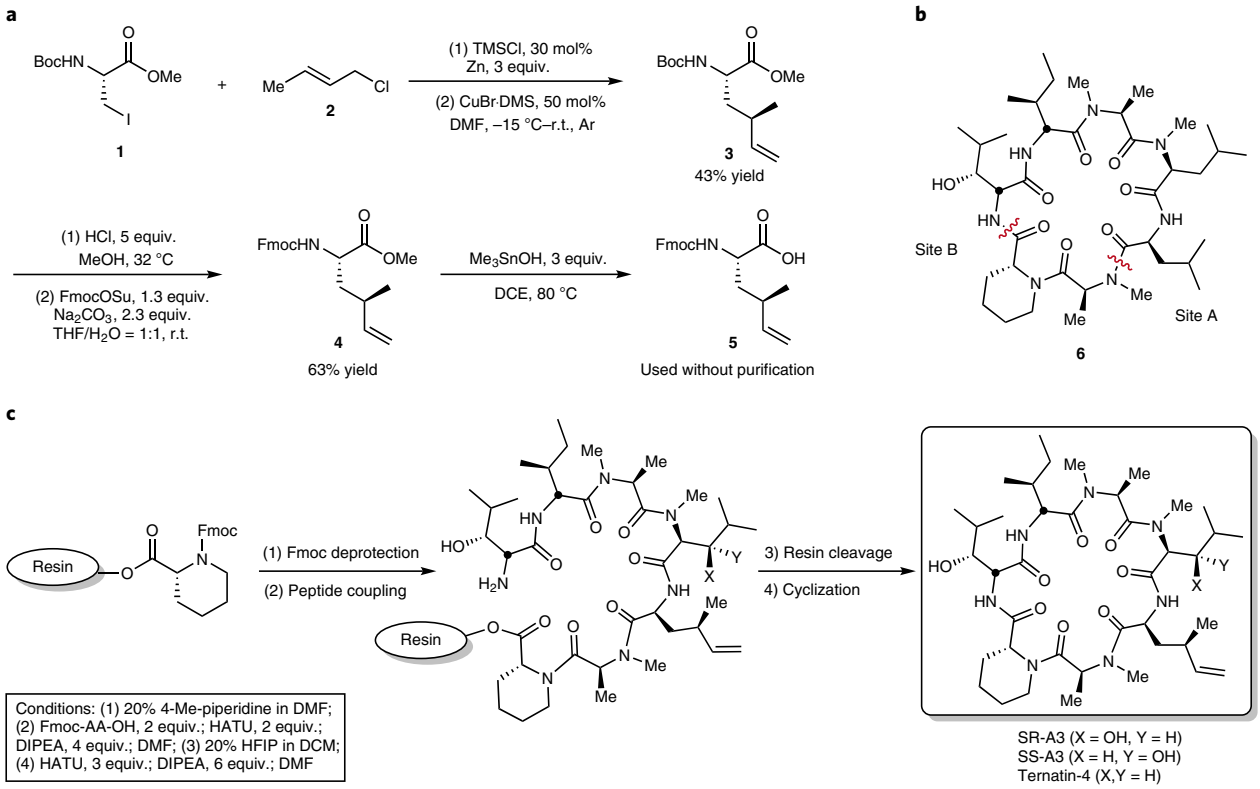

Fig. 2 | Expeditious synthesis of dhML, ternatin-4 and A3 epimers. a, Scheme for synthesis of Fmoc-dhML **5**. Su, succinimide; THF, tetrahydrofuran; r.t., room temperature; TMSCl, trimethylsilyl chloride; DMF, N, N-Dimethylformamide; DCE, 1,2-Dichloroethane. **b**, Identification of alternative macrocyclization site B. **c**, Scheme for solid-phase synthesis of linear heptapeptide precursors, followed by solution-phase cyclization to provide ternatin-4, SR-A3 and SS-A3 (Supplementary Information for details). AA, amino acid; HATU, 1-[Bis(dimethylamino)methylene]-1H-1,2,3-triazolo[4,5-b] pyridinium 3-oxid hexafluorophosphate; DIPEA, N,N-Diisopropylethylamine; HFIP, 1,1,1,3,3,3-Hexafluoro-2-propanol; DCM, dichloromethane.

rates recovered nearly to DMSO control levels after transient exposure to 100 nM ternatin-4 or SS-A3 (Fig. 4d). These results demonstrate that the (*R*)-β-hydroxy group attached to *N*-Me-Leu endows SR-A3 with a substantial kinetic advantage over SS-A3 and ternatin-4, as reflected by the wash-out resistance and increased cellular residence time associated with inhibition of protein synthesis and cell proliferation.

Single-molecule FRET imaging reveals enhanced residence time and rebinding kinetics of SR-A3. To gain mechanistic insight into SR-A3's kinetic advantage in cells relative to ternatin-4 and SS-A3, we employed smFRET imaging of biochemically reconstituted, eEF1A-catalysed translation reactions[22]. In this assay, tRNA in the P site of surface-immobilized human ribosomes is labelled with a donor fluorophore (Cy3) (Fig. 5a). Aminoacylated tRNA labelled with an acceptor fluorophore (LD655) is then stopped-flow delivered as a ternary complex (TC) with eEF1A and GTP. The resulting reaction is monitored in real time using a home-built total internal reflection microscope[23]. The FRET efficiency between the two fluorophores—inversely related to the distance between the two tRNAs—increases through a series of well-characterized states (Fig. 5a): initiation complex (**IC**), GTPase-activated (**GA**) and fully accommodated (**AC**)[22,24].

Before TC addition, no FRET is observed (Fig. 5a, **IC**; Fig. 5b). When TC is introduced to the microscope flow cell, it binds rapidly to the ribosomal A site, where codon–anticodon recognition occurs (Fig. 5a, **GA**), resulting in GTP hydrolysis and subsequent dissociation of eEF1A from aa-tRNA and the ribosome. The ribosome complex exhibits similar time-averaged FRET efficiencies of ~0.5 at both **GA** states (before and immediately after eEF1A dissociation). Upon eEF1A dissociation, aa-tRNA accommodates into the ribosomal peptidyl transferase centre (Fig. 5a, **AC**), as revealed by the marked increase in FRET efficiency to ~0.7 in DMSO control reactions (Fig. 5b, left). By contrast, when TC was delivered in the presence of 10 μM ternatin-4, SS-A3 or SR-A3, aa-tRNA accommodation was strongly inhibited, whereas formation of the initial TC/ribosome intermediate was unaffected (Fig. 5b). These results suggest that all three compounds similarly stall elongating ribosomes bound to TC (Fig. 5a, **GA**), presumably by preventing conformational changes in eEF1A (either before or after GTP hydrolysis), which are required for its dissociation from aa-tRNA and the ribosome.

Since SR-A3 exhibited a greater cellular residence time than ternatin-4 or SS-A3 (Fig. 4e), we designed a series of in vitro chase experiments to quantify differences in dissociation rates and rebinding constants between these closely related analogues. We first generated a population of drug-stalled elongation complexes by incubating immobilized ribosomes with TC and 10 μM of each drug for 30 seconds. Excess TC and drugs were then washed out of the microscope flow cell with buffer containing 0, 2.5, 5, 7.5 or 10 μM drug at the start of data acquisition. Under these wash-out conditions, drug-stalled elongation complexes can gradually transition into the fully accommodated high-FRET state (Fig. 5c, example trace showing wash-out into drug-free buffer). We estimated the average time required for aa-tRNA accommodation to occur in each wash-out condition (t_{acc}) from cumulative dwell-time distributions by calculating the fraction of ribosomes that reached the high-FRET state at each time point and fitting exponential functions to the resulting data (Fig. 5d and Extended Data Fig. 4a; Methods for details).

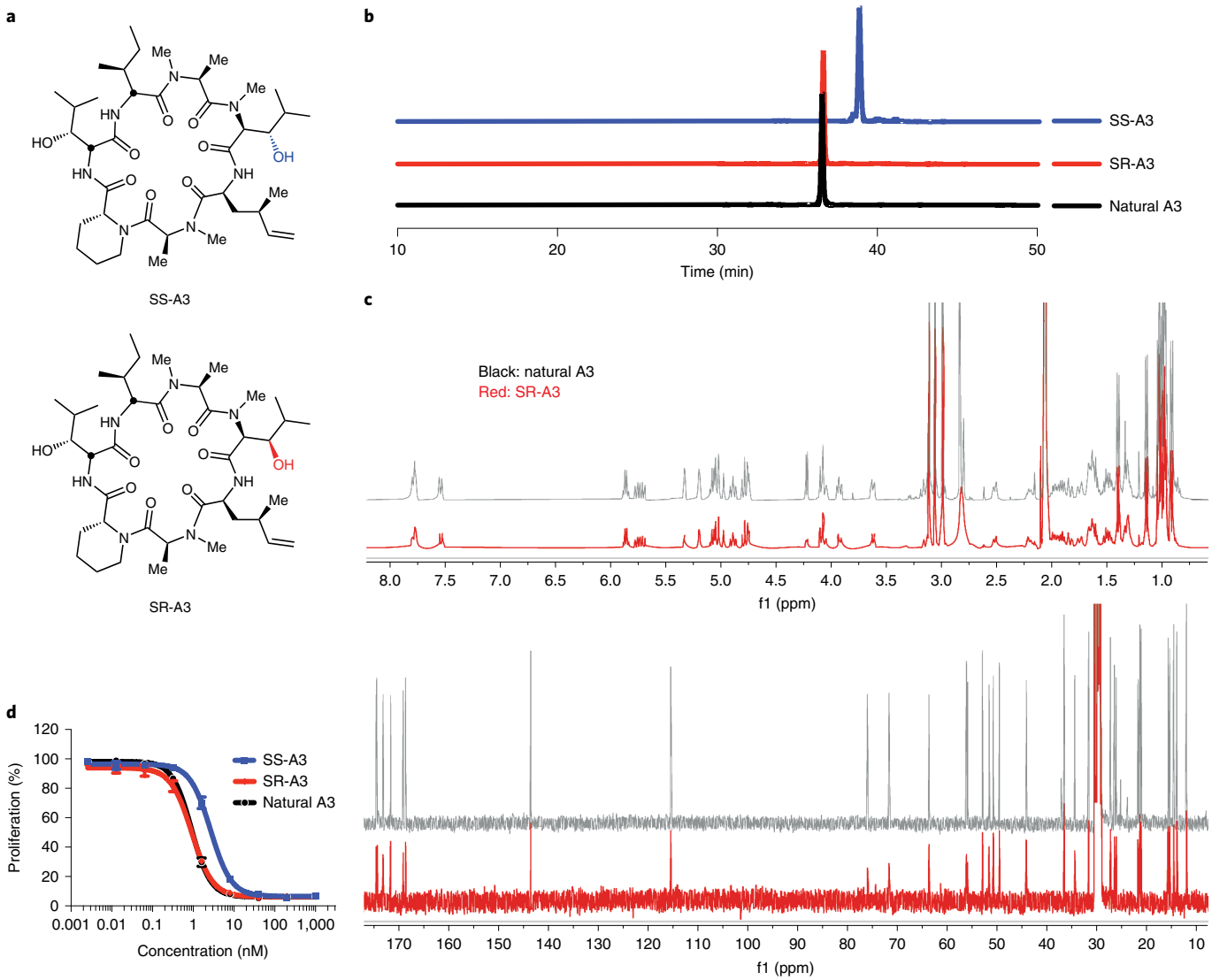

Fig. 3 | SR-A3 is indistinguishable from naturally derived A3. a, Chemical structures of SS-A3 and SR-A3. **b**, HPLC elution profiles. **c**, Overlay of ^{1}H (top) and ^{13}C (bottom) NMR spectra in acetone-d_6. f1, the resolution of the indirect dimension. **d**, Concentration-dependent anti-proliferative effects in HCT116 cells after 72 h. Cell proliferation (percent DMSO control) was quantified using alamarBlue. Data points (percent DMSO control) are mean values ± s.d. ($n = 3$).

Given the assumption that drug dissociation must occur prior to aa-tRNA accommodation, the drug residence times and rebinding constants can then be determined from the chase series (Fig. 5e; Methods for details)[25,26]. Based on the measured inhibition time after wash-out into drug-free buffer, the residence time of SR-A3 (82 s) is about 60% longer than that of ternatin-4 (56 s) or SS-A3 (51 s). In addition, the rebinding constant, which corresponds to the drug concentration in the wash-out buffer required to double the inhibition time (relative to drug-free buffer) through drug rebinding events, strongly favours SR-A3 (Fig. 5e). This implies that SR-A3 rebinds to the stalled eEF1A–ribosome complex (**GA** or related states; Fig. 5a) twice as fast as SS-A3 and four times as fast as ternatin-4 (Fig. 5e and Extended Data Fig. 4b). Taken together, and consistent with our cell-based findings, our smFRET data show that (*S,R*)-*N*-Me-β-OH-Leu stereospecifically endows SR-A3 with a longer residence time and faster target rebinding kinetics upon dissociation.

SR-A3 treatment significantly extends survival of Eμ-Myc tumour-bearing mice. The oncogenic transcription factor Myc is dysregulated in >50% of human cancers[27]. Structural alterations of the *MYC* gene cause B-cell lymphoma in humans and mice[28–31], and a Myc-dependent increase in protein synthesis is a key oncogenic determinant[32]. The Eμ-Myc transgenic mouse[28], in which Myc is specifically overexpressed in B lymphocytes, has been employed as a preclinical model of human Burkitt lymphoma and other Myc-driven B-cell malignancies. Hence, the Eμ-Myc model is a paradigm for testing whether inhibition of protein synthesis downstream of Myc oncogenic activity confers therapeutic benefit. Given its enhanced residence time and rebinding kinetics, as well as improved metabolic stability (Extended Data Fig. 5a), we selected SR-A3 for a preclinical trial using the Eμ-Myc lymphoma allograft model. After intravenous injection of wild-type immunocompetent mice with mouse Eμ-Myc/+ lymphoma cells and waiting until tumours were palpable (approximately two weeks after injection), we began treatment with either vehicle or SR-A3 (dosed three times per week, 1.5 or 2.0 mg kg^{-1}, by intraperitoneal injection). Treatment of tumour-bearing mice with single-agent SR-A3 dramatically prolonged survival in a dose-dependent manner (Fig. 6a). Moreover, SR-A3 was well tolerated in both dose groups, and no notable body weight loss was observed (Extended Data Fig. 5b).

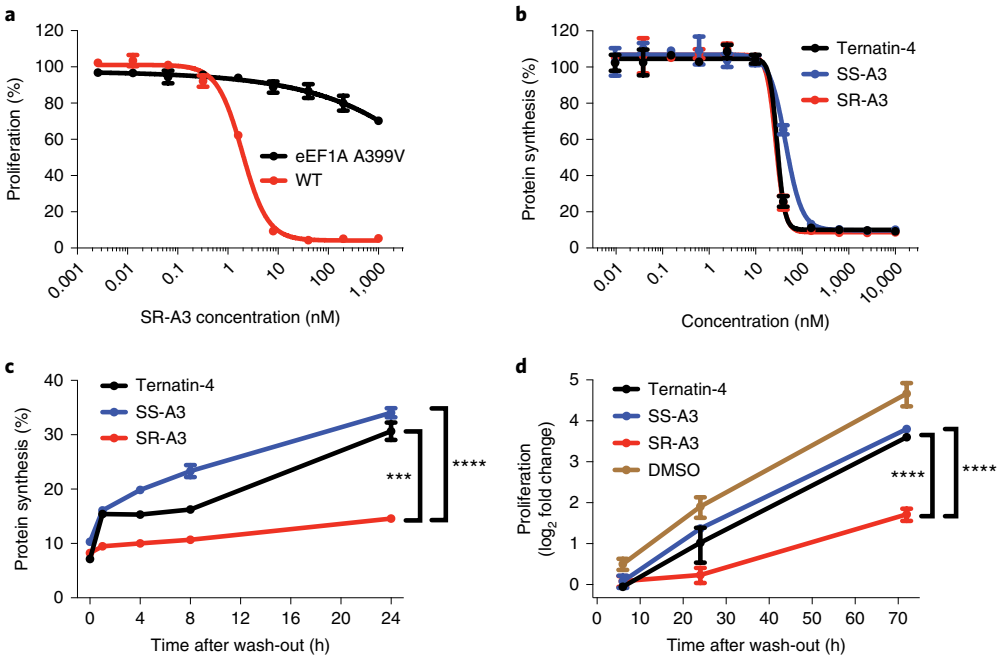

Fig. 4 | *N*-Me-β-OH-Leu stereospecifically endows SR-A3 with increased cellular residence time. a, Wild-type (WT) and eEF1A-mutant (A399V) HCT116 cells were treated with SR-A3 for 72 h. Cell proliferation (percent DMSO control) was quantified using alamarBlue. Data points are mean values ± s.d. ($n = 3$). **b**, HCT116 cells were treated with the indicated compounds for 24 h and protein synthesis was quantified after pulse labelling with OPP for 1 h (Methods). Data points (percent DMSO control) are mean values ± s.d. ($n = 3$). **c**, HCT116 cells were treated with the indicated compounds (100 nM) or DMSO for 4 h, followed by wash-out into compound-free media. At the indicated time points post-wash-out, cells were pulse-labelled with OPP (1 h), and OPP incorporation was quantified. Normalized data (percent DMSO control) are mean values ± s.d. ($n = 3$). Statistical significance was determined by one-way analysis of variance (ANOVA) followed by Sidak's multiple comparisons test. ***$P < 0.001$; ****$P < 0.0001$. The P value for SR-A3 versus ternatin-4 is 0.0001. The P value for SR-A3 versus SS-A3 is <0.0001. **d**, HCT116 cells were treated with the indicated compounds (100 nM) or DMSO for 4 h, followed by wash-out into compound-free media. At the indicated time points post-wash-out, cell proliferation was quantified using the CellTiter-Glo assay. Normalized data ($\log_2$ fold change versus DMSO control at time $t = 0$ h post-wash-out) are mean values ± s.d. ($n = 3$). Statistical significance was determined by one-way ANOVA followed by Sidak's multiple comparisons test. ****$P < 0.0001$. The P value for SR-A3 versus ternatin-4 is <0.0001. The P value for SR-A3 versus SS-A3 is <0.0001.

Having established an efficacious and well-tolerated dosing regimen for SR-A3, we sought to test whether its enhanced residence time relative to ternatin-4 translates to improved antitumour activity in vivo. To ensure a fair comparison in the head-to-head antitumour study, we first assessed the pharmacokinetics of each compound in mice (2 mg kg^{-1}, single intraperitoneal injection). The area under the plasma concentration-time curve (AUC_{inf}) for SR-A3 was ~2.1-fold higher than for ternatin-4 (Fig. 6b), and the maximum plasma concentration (C_{max}) was ~1.7-fold higher (Extended Data Fig. 6a). We therefore treated Eμ-Myc tumour-bearing mice with either vehicle, 4.2 mg kg^{-1} ternatin-4 or 2 mg kg^{-1} SR-A3 (three times per week, $n = 5$ mice per treatment arm). After two weeks of treatment, tumours from each mouse were collected and weighed. Strikingly, SR-A3 treatment significantly reduced tumour burden, whereas ternatin-4 had no significant effect (Fig. 6c and Extended Data Fig. 6b,c). These results demonstrate the clear improvement in antitumour efficacy conferred by (*R*)-β-OH-*N*-Me-Leu and suggest that SR-A3 may be a viable preclinical candidate for the treatment of Myc-driven B lymphoid tumours.

Discussion

In this study, we first developed an improved synthetic route to dhML-containing ternatin variants, culminating in the total syntheses of SR-A3 and SS-A3 (Fig. 2). Our work provides spectroscopic, chromatographic and pharmacological evidence that synthetic SR-A3 (and not SS-A3) is identical to the fungal natural product 'A3' (Fig. 3), confirming the previous partial structure elucidation and providing a complete stereochemical assignment of this potent eEF1A antagonist.

SR-A3 differs structurally from the previously reported eEF1A inhibitor, ternatin-4, by the addition of a single oxygen atom into the side chain of *N*-Me-Leu (Fig. 1). We speculate that A3 is evolutionarily related to ternatin via acquisition of biosynthetic modules for (*R*)-pipecolic acid and (*S*,*R*)-dhML, as well as stereospecific hydroxylation of *N*-Me-Leu by the A3-producing fungus. Although amino acid β-hydroxylation is a common biosynthetic modification in cyclic peptide natural products, its stereospecific functions are mostly unknown. An unexpected finding from our work is that the *N*-Me-Leu β-hydroxyl in SR-A3 has little effect on cellular potency under continuous treatment conditions, as compared with ternatin-4. Rather, the β-hydroxyl in SR-A3, but not SS-A3, confers a dramatic increase in drug-target residence time and rebinding kinetics, as revealed by wash-out experiments in cells and reconstituted eEF1A-catalysed elongation reactions monitored by smFRET (Fig. 4c,d and Fig. 5). We note that 'drug-target residence time' measured in cells and tissues is determined by both drug dissociation and rebinding kinetics. Moreover, the intracellular concentration (or local density) of the target can play a major role in drug rebinding kinetics[20]. This can potentially explain the much longer residence time in cells, where [eEF1A] is ~35 μM (ref. [33]), as compared to the smFRET flow cell, where [eEF1A] is ≪10 nM post-wash-out. The structural basis of SR-A3's enhanced binding kinetics will likely require cryo-electron microscopy analysis of stalled SR-A3/eEF1A/ribosome complexes at atomic resolution. Although the precise molecular mechanism by which the β-hydroxyl confers this kinetic advantage awaits further investigation, our study nevertheless reveals the power of smFRET imaging to illuminate differences

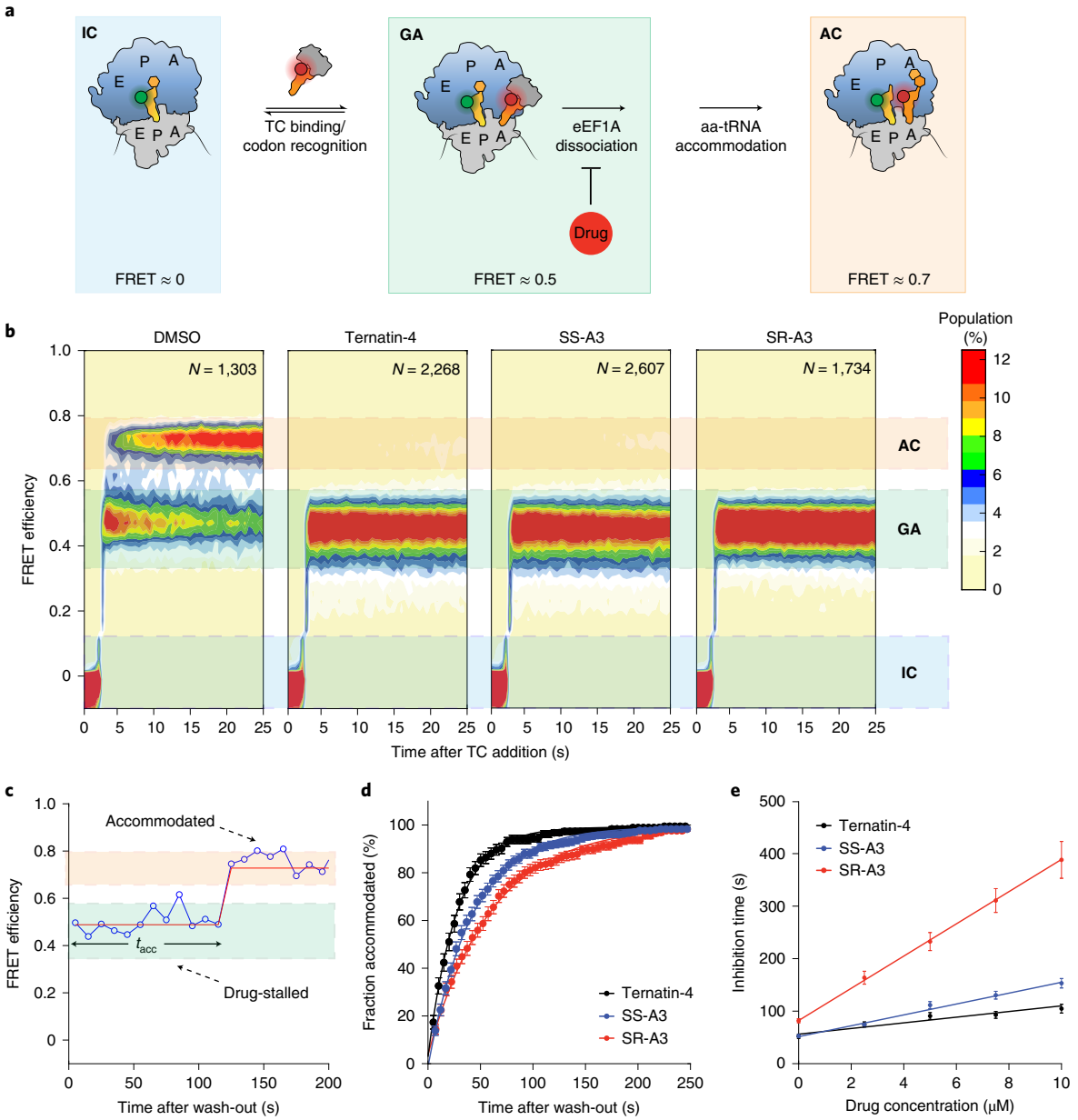

Fig. 5 | Single-molecule FRET imaging reveals increased residence time and rebinding kinetics of SR-A3. a, Schematic showing predominant long-lived reaction species (**IC**, **GA** and **AC**) detected by the experimental set-up. E, exit; P, peptidyl; A, aminoacyl. **b**, Population FRET histograms of reactions initiated from **IC** by delivering the TC and either DMSO or the indicated drug (10 μM) at the start of data acquisition. *N*, number of observed molecules. **c**, Representative smFRET trace from a chase experiment initiated from drug-stalled elongation complexes (**GA**) by pre-incubation with SR-A3, followed by wash-out into drug-free buffer at the start of data acquisition. Blue circles represent the measured FRET efficiency for each video frame; the solid red line represents a hidden Markov model idealization of the data. **d**, Cumulative drug dissociation time distributions constructed from several thousand FRET traces as in **c** after wash-out into drug-free buffer. Data points represent bootstrap means (±s.e.m.) from all FRET traces acquired in a single video. The solid lines represent fits of single-exponential functions to the data ($n = 3$). **e**, Plots of inhibition time (prior to accommodation) as a function of drug concentration in the wash-out buffer were used to determine drug residence times and rebinding constants. Inhibition times were derived from curves shown in **d**, after wash-out into buffer containing the indicated drug concentrations. Each data point represents the mean of three independent experiments (±s.e.m., $n = 3$). Solid lines are linear fits to the data, with adjusted $R^2 = 0.90$ (ternatin-4), 0.98 (SS-A3) and 0.99 (SR-A3). R^2, coefficient of determination.

in drug dissociation and rebinding kinetics, both of which can contribute to drug-target residence time and therapeutic efficacy[20].

Dysregulation of the transcription factor Myc underlies multiple human cancers[27]. Nevertheless, Myc is still considered 'undruggable' and no direct Myc inhibitors have advanced into clinical trials. Because the oncogenic activity of Myc relies on its ability to promote ribosome biogenesis and protein synthesis, an alternative approach is to attenuate protein synthesis rates. The Eμ-Myc lymphoma model has been employed to test various protein synthesis inhibition strategies, often in combination with other cytotoxic drugs. Targeting the protein synthesis machinery in Eμ-Myc mice either genetically[32] or pharmacologically[34–36] has been shown to suppress tumour growth and prolong overall survival. However, to the best of our knowledge, no translation elongation inhibitors have shown single-agent efficacy in this aggressive B-cell lymphoma model.

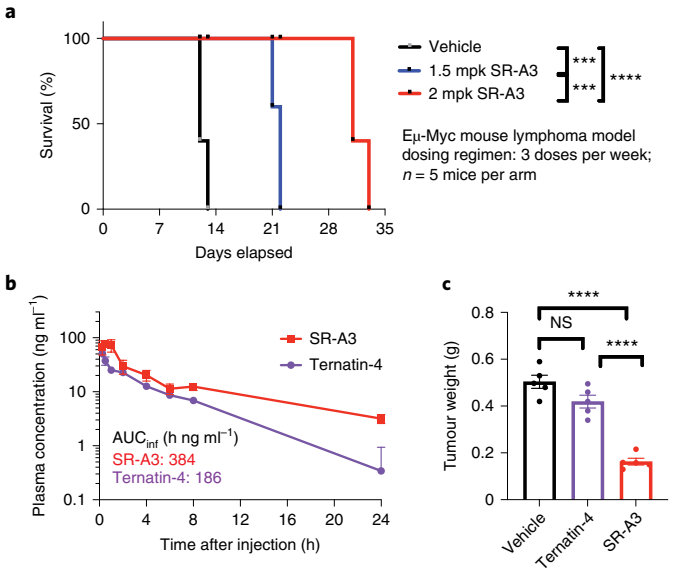

Fig. 6 | SR-A3 extends overall survival and reduces tumour burden in the Eμ-Myc mouse lymphoma model. a, Kaplan–Meier survival curves for mice dosed with vehicle or the indicated doses of SR-A3 (intraperitoneal injection, three times per week, $n = 5$ per dose group). Day 0 indicates the beginning of treatment. Statistical significance was determined by logrank test. ***$P < 0.001$; ****$P < 0.0001$. The P value for 2 mg per kg (mpk) SR-A3 versus vehicle is <0.0001. The P value for 2 mpk SR-A3 versus 1.5 mpk SR-A3 is 0.0001. The P value for 1.5 mpk SR-A3 versus vehicle is 0.0002. **b**, Mouse plasma concentrations of SR-A3 or ternatin-4 after intraperitoneal injection at 2 mg kg^{-1} (mean ± s.d., $n = 3$ mice per time point). **c**, Tumour weights from Eμ-Myc mice after two weeks of treatment with vehicle, ternatin-4 (4.2 mg kg^{-1}) or SR-A3 (2 mg kg^{-1}; $n = 5$ per group). Graph represents mean value ± s.d. Statistical significance was determined by one-way ANOVA followed by Sidak's multiple comparisons test. NS, not significant; ****$P < 0.0001$. The P value for SR-A3 versus vehicle is <0.0001. The P value for SR-A3 versus ternatin-4 is <0.0001. The P value for ternatin-4 versus vehicle is 0.0708.

Our preclinical trial revealed that intermittent, low doses of SR-A3 (1.5–2.0 mg kg^{-1}, three times per week), but not the des-OH (no hydroxyl) variant ternatin-4, profoundly reduced tumour burden and extended the survival of Eμ-Myc mice without obvious toxicity (Fig. 6). SR-A3 thus shows therapeutic potential for the treatment of Myc-driven B-cell lymphoma. Our study of SR-A3 chemistry and biology provides a compelling illustration of how a 'ligand efficient' side-chain modification (one oxygen atom) can be exploited to alter the pharmacological properties and residence time of a cyclic peptide natural product.

Online content

Any methods, additional references, Nature Research reporting summaries, source data, extended data, supplementary information, acknowledgements, peer review information; details of author contributions and competing interests; and statements of data and code availability are available at https://doi.org/10.1038/s41557-022-01039-3.

Received: 11 September 2021; Accepted: 8 August 2022;
Published online: 19 September 2022

References

1. Lin, J., Zhou, D., Steitz, T. A., Polikanov, Y. S. & Gagnon, M. G. Ribosome-targeting antibiotics: modes of action, mechanisms of Resistance, and implications for Drug design. *Annu. Rev. Biochem.* **87**, 451–478 (2018).
2. Xu, Y. & Ruggero, D. The role of translation control in tumorigenesis and its therapeutic implications. *Annu. Rev. Cancer Biol.* **4**, 437–457 (2020).
3. Fan, A. & Sharp, P. P. Inhibitors of eukaryotic translational machinery as therapeutic agents. *J. Med. Chem.* **64**, 2436–2465 (2021).
4. Schuller, A. P. & Green, R. Roadblocks and resolutions in eukaryotic translation. *Nat. Rev. Mol. Cell Biol.* **19**, 526–541 (2018).
5. Abbas, W., Kumar, A. & Herbein, G. The eEF1A proteins: at the crossroads of oncogenesis, apoptosis, and viral infections. *Front. Oncol.* **5**, 75 (2015).
6. Crews, C. M., Collins, J. L., Lane, W. S., Snapper, M. L. & Schreiber, S. L. GTP-dependent binding of the antiproliferative agent didemnin to elongation factor 1 alpha. *J. Biol. Chem.* **269**, 15411–15414 (1994).
7. Shao, S. et al. Decoding mammalian ribosome-mRNA states by translational GTPase complexes. *Cell* **167**, 1229–1240.e1215 (2016).
8. Lindqvist, L. et al. Inhibition of translation by cytotrienin A—a member of the ansamycin family. *RNA* **16**, 2404–2413 (2010).
9. Krastel, P. et al. Nannocystin A: an elongation factor 1 inhibitor from myxobacteria with differential anti-cancer properties. *Angew. Chem. Int. Ed.* **54**, 10149–10154 (2015).
10. Klein, V. G. et al. Identifying the cellular target of cordyheptapeptide A and synthetic derivatives. *ACS Chem. Biol.* **16**, 1354–1364 (2021).
11. Spicka, I. et al. Randomized phase III study (ADMYRE) of plitidepsin in combination with dexamethasone vs. dexamethasone alone in patients with relapsed/refractory multiple myeloma. *Ann. Hematol.* **98**, 2139–2150 (2019).
12. White, K. M. et al. Plitidepsin has potent preclinical efficacy against SARS-CoV-2 by targeting the host protein eEF1A. *Science* **371**, 926–931 (2021).
13. Blunt, J. et al. Bioactive compounds. International patent WO 2010/062159 A1 (2010).
14. Shimokawa, K. et al. (−)-Ternatin, a highly N-methylated cyclic heptapeptide that inhibits fat accumulation: structure and synthesis. *Tetrahedron Lett.* **47**, 4445–4448 (2006).
15. Carelli, J. D. et al. Ternatin and improved synthetic variants kill cancer cells by targeting the elongation factor-1A ternary complex. *Elife* **4**, e10222 (2015).
16. Gordon, D. E. et al. A SARS-CoV-2 protein interaction map reveals targets for drug repurposing. *Nature* **583**, 459–468 (2020).
17. Deboves, H. J. C., Grabowska, U., Rizzo, A. & Jackson, R. F. W. A new route to hydrophobic amino acids using copper-promoted reactions of serine-derived organozinc reagents. *J. Chem. Soc. Perkin Trans. 1* **2000**, 4284–4292 (2000).
18. Dunn, M. J., Jackson, R. F. W., Pietruszka, J. & Turner, D. Synthesis of enantiomerically pure unsaturated alpha-amino acids using serine-derived zinc/copper reagents. *J. Org. Chem.* **60**, 2210–2215 (1995).
19. Liu, J., Xu, Y., Stoleru, D. & Salic, A. Imaging protein synthesis in cells and tissues with an alkyne analog of puromycin. *Proc. Natl Acad. Sci. USA* **109**, 413–418 (2012).
20. Vauquelin, G. Rebinding: or why drugs may act longer *in vivo* than expected from their *in vitro* target residence time. *Expert Opin. Drug Discov.* **5**, 927–941 (2010).
21. Copeland, R. A. The drug-target residence time model: a 10-year retrospective. *Nat. Rev. Drug Discov.* **15**, 87–95 (2016).
22. Ferguson, A. et al. Functional dynamics within the human ribosome regulate the rate of active protein synthesis. *Mol. Cell* **60**, 475–486 (2015).
23. Juette, M. F. et al. Single-molecule imaging of non-equilibrium molecular ensembles on the millisecond timescale. *Nat. Methods* **13**, 341–344 (2016).
24. Geggier, P. et al. Conformational sampling of aminoacyl-tRNA during selection on the bacterial ribosome. *J. Mol. Biol.* **399**, 576–595 (2010).
25. Borg, A. et al. Fusidic acid targets elongation factor G in several stages of translocation on the bacterial ribosome. *J. Biol. Chem.* **290**, 3440–3454 (2015).
26. Holm, M., Borg, A., Ehrenberg, M. & Sanyal, S. Molecular mechanism of viomycin inhibition of peptide elongation in bacteria. *Proc. Natl Acad. Sci. USA* **113**, 978–983 (2016).
27. Gabay, M., Li, Y. & Felsher, D. W. MYC activation is a hallmark of cancer initiation and maintenance. *Cold Spring Harb. Perspect. Med.* **4**, a014241 (2014).
28. Harris, A. W. et al. The E mu-myc transgenic mouse. A model for high-incidence spontaneous lymphoma and leukemia of early B cells. *J. Exp. Med.* **167**, 353–371 (1988).
29. Gelmann, E. P., Psallidopoulos, M. C., Papas, T. S. & Dalla-Favera, R. Identification of reciprocal translocation sites within the c-*myc* oncogene and immunoglobulin μ locus in a Burkitt lymphoma. *Nature* **306**, 799–803 (1983).
30. Reddy, A. et al. Genetic and functional drivers of diffuse large B cell lymphoma. *Cell* **171**, 481–494.e415 (2017).
31. Chapuy, B. et al. Molecular subtypes of diffuse large B cell lymphoma are associated with distinct pathogenic mechanisms and outcomes. *Nat. Med.* **24**, 679–690 (2018).
32. Barna, M. et al. Suppression of Myc oncogenic activity by ribosomal protein haploinsufficiency. *Nature* **456**, 971–975 (2008).
33. Itzhak, D. N., Tyanova, S., Cox, J. & Borner, G. H. Global, quantitative and dynamic mapping of protein subcellular localization. *Elife* **5**, e16950 (2016).

34. Pourdehnad, M. et al. Myc and mTOR converge on a common node in protein synthesis control that confers synthetic lethality in Myc-driven cancers. *Proc. Natl Acad. Sci. USA* **110**, 11988–11993 (2013).
35. Robert, F. et al. Altering chemosensitivity by modulating translation elongation. *PLoS ONE* **4**, e5428 (2009).
36. Bordeleau, M. E. et al. Therapeutic suppression of translation initiation modulates chemosensitivity in a mouse lymphoma model. *J. Clin. Investig.* **118**, 2651–2660 (2008).

Methods

Cell culture. HCT116 cells (ATCC) were maintained in McCoy's 5A media (Gibco) supplemented with 10% foetal bovine serum (FBS; Axenia Biologix), 100 units ml^{-1} penicillin and 100 µg ml^{-1} streptomycin (Gibco). H929 cells (ATCC) were maintained in advanced RPMI 1640 media (Gibco) supplemented with 6% FBS, 2 mM glutamine, 100 units ml^{-1} penicillin and 100 mg ml^{-1} streptomycin. MM1S, Jurkat and Ramos cells (ATCC) were maintained in RPMI 1640 media (Gibco) supplemented with 10% FBS, 100 units ml^{-1} penicillin and 100 mg ml^{-1} streptomycin. All cells were cultured at 37 °C in a 5% CO_2 atmosphere.

The natural product A3 was purified as described previously[13].

Proliferation assay. Adherent cells were briefly trypsinized and repeatedly pipetted to produce a homogeneous cell suspension. 2,500 cells were seeded in 100 µl complete growth media per well in 96-well clear-bottom plates. Suspension cells were repeatedly pipetted to produce a homogeneous cell suspension. 10,000 cells were seeded in 100 µl complete growth media per well in 96-well clear-bottom plates. After allowing cells to grow/adhere overnight, cells were treated with 25 µl per well of ×5 drug stocks (0.1% DMSO final) and incubated for 72 hours. AlamarBlue (Life Technologies) was used to assess cell viability per the manufacturer's instructions. Briefly, 12.5 µl alamarBlue reagent was added to each well, and plates were incubated at 37 °C. Fluorescence intensity was measured every 30 min to determine the linear range for each assay (excitation (Ex), 545 nm; emission (Em), 590 nm; SPARK, Tecan Austria). Proliferation curves were generated by first normalizing fluorescence intensity in each well to the DMSO-treated plate average. Normalized fluorescence intensity was plotted in GraphPad Prism (GraphPad), and IC_{50} values were calculated from nonlinear regression curves. The reported IC_{50} values represent the average of at least three independent determinations (±s.d.).

Wash-out proliferation assay. Adherent cells were briefly trypsinized and repeatedly pipetted to produce a homogeneous cell suspension. 2,500 cells were seeded in 100 µl complete growth media per well in 96-well clear-bottom plates. After allowing cells to grow/adhere overnight, cells were treated with ternatin analogues (100 nM, 0.1% DMSO final) and incubated for the indicated times. The growth medium was carefully removed, cells were washed with warm phosphate buffered saline (PBS) twice (×2 short wash), followed by 5 min incubation in warm media at 37 °C (long wash). This 'short–long' washing cycle was repeated three times. After indicated times post-wash-out, CellTiter-Glo (Promega) was used to assess cell viability per the manufacturer's instructions. Briefly, after adding 100 µl CellTiter-Glo reagent to each well, the plate was rocked at room temperature for 5–10 min, and the luminescence intensity was measured. Proliferation curves were generated by first normalizing luminescence intensity in each well to the average values from the $t=0$ time point. Normalized luminescence intensity was plotted in GraphPad Prism (GraphPad). The reported values represent the average of at least three independent determinations (±s.d.). Statistical significance was determined by one-way ANOVA followed by Sidak's multiple comparisons test.

OPP incorporation assay. HCT116 cells at 60% confluency in 12-well plates were incubated with the indicated concentrations of ternatin analogues for 10 min or 24 h at 37 °C. After the indicated times, OPP (30 µM final concentration) was added, and the cells were incubated for 1 hour at 37 °C. Subsequently, the medium was removed, and the cells were trypsinized, collected and washed twice with ice-cold PBS before transferring to a 96-well V-bottom plate. 100 µl Zombie Green (BioLegend) solution was added to each well and incubated for 30 min at room temperature in the dark. Cells were then washed with 2% FBS in PBS before fixation with 200 µl of 4% paraformaldehyde (PFA) in PBS for 15 min on ice in the dark. After washing the cells with 2% FBS in PBS, 200 µl permeabilization buffer (3% FBS, 0.1% saponin in PBS) was added to each well, and the cells were incubated for 5 min at room temperature in the dark. Cells were then washed and resuspended in 25 µl permeabilization buffer. 100 µl click chemistry mix (50 mM HEPES buffer (pH 7.5), 150 mM NaCl, 400 µM tris(2-carboxyethyl) phosphine (TCEP), 250 µM tris((1-benzyl-4-triazolyl)methyl)amine (TBTA), 5 µM CF647-Azide red dye (Biotium) and 200 µM $CuSO_4$) was added to each well, and cells were incubated at room temperature in the dark. After overnight incubation, the cells were washed with permeabilization buffer followed by Flow Cytometry Staining Buffer (FACS buffer) (2% FBS, 1% penicillin/streptomycin (P/S) and 2 mM ethylenediaminetetraacetic acid (EDTA), in PBS without Ca/Mg). Cells were then resuspended in 200 µl FACS buffer and filtered before FACS analysis (CytoFLEX, Beckman-Coulter; FlowJo v.10.7.1, BD). Supplementary Fig. 1 shows the gating strategy. Protein synthesis inhibition curves were generated by gating for single live cells and plotting mean fluorescence intensity relative to the DMSO control values using GraphPad Prism (GraphPad). IC_{50} values were calculated from nonlinear regression curves. The reported values represent the average of at least three independent determinations (±s.d.).

Wash-out OPP assay. HCT116 cells at 60% confluency in 12-well plates were incubated with compounds at 100 nM for 4 h at 37 °C. The medium was carefully removed, and cells were washed with warm PBS twice (×2 short wash), followed by 5 min incubation in warm media at 37 °C (long wash). After repeating the short–long wash-out cycle three times, cells were resuspended in warm media and incubated at 37 °C. After the indicated times post-wash-out, OPP (30 µM final concentration) was added, and the cells were incubated for an additional 1 h at 37 °C. The medium was removed, and the cells were trypsinized, collected, and washed twice with ice-cold PBS before transferring to a 96-well V-bottom plate. 100 µl Zombie Green (BioLegend) solution was added to each well and incubated for 30 min at room temperature in the dark. Cells were then washed with 2% FBS in PBS before fixation with 200 µl of 4% PFA in PBS for 15 min on ice in the dark. After washing the cells with 2% FBS in PBS, 200 µl permeabilization buffer (3% FBS, 0.1% saponin in PBS) was added to each well, and cells were incubated for 5 min at room temperature in the dark. Cells were then washed and resuspended in 25 µl permeabilization buffer. 100 µl click chemistry mix (50 mM HEPES (pH 7.5), 150 mM NaCl, 400 µM TCEP, 250 µM TBTA, 5 µM CF647-Azide (Biotium) and 200 µM $CuSO_4$) was added to each well, and cells were incubated at room temperature in the dark. After the overnight incubation, cells were washed with permeabilization buffer followed by FACS buffer (2% FBS, 1% P/S and 2 mM EDTA, in PBS without Ca/Mg). Cells were then resuspended in 200 µl FACS buffer and filtered before FACS analysis as described above. Statistical significance was determined by one-way ANOVA followed by Sidak's multiple comparisons test.

The smFRET data collection. Ribosomes from HEK293T cells, elongation factor eEF1A and fluorescence-labelled tRNAs were prepared using the protocol described previously[37]. All smFRET experiments were carried out at 25 °C in human polymix buffer (20 mM HEPES (pH 7.5), 5 mM $MgCl_2$, 140 mM KCl, 10 mM NH_4Cl, 2 mM spermidine, 5 mM putrescine and 1.5 mM 2-mercaptoethanol) containing 500 µM cycloheximide and a mixture of triplet-state quenchers (1 mM trolox, 1 mM 4-nitrobenzyl alcohol, 1 mM cyclooctatetraene) and an enzymatic oxygen scavenging system (2 µM 3,4-dihydroxybenzoic acid, 0.02 units ml^{-1} protocatechuate 3,4-dioxygenase). The time evolution of the FRET signal was recorded using a home-built total-internal-reflection-based fluorescence microscope at ~0.1 kW cm^{-2} laser illumination (532 nm). Videos were recorded either in time-lapse mode with one 500 ms frame acquired every 10 seconds or continuously at a time resolution of 500 ms. Donor and acceptor fluorescence intensities were extracted from the recorded videos, and FRET efficiency traces were calculated using the SPARTAN software package[23]. FRET traces were selected for further analysis according to the following criteria: a single catastrophic photobleaching event, at least 8:1 signal/background-noise ratio and 6:1 signal/signal-noise ratio, less than four donor-fluorophore blinking events and a correlation coefficient between donor and acceptor of <0.5. The resulting smFRET traces were analysed using hidden Markov model idealization methods as implemented in the SPARTAN software package[23].

Ternary complex real-time delivery experiments. Some 80S initiation complexes containing Met-$tRNA^{fMet}$-Cy3 and displaying the codon UUC in the A site were immobilized on passivated quartz slides as described previously[37,38]. This was followed by delivery of 10 nM eEF1A ternary complex containing Phe-$tRNA^{Phe}$-LD655 together with 1 mM GTP and either DMSO or 10 µM drug at the start of data acquisition.

Drug chase experiments. Stalled pre-accommodation complexes were formed by immobilization of 80S initiation complexes containing Met-$tRNA^{fMet}$-Cy3 and displaying the codon UUC in the A site to passivated quartz slides as described previously[37,38], followed by delivery of 10 nM eEF1A ternary complex containing Phe-$tRNA^{Phe}$-LD655 together with 1 mM GTP and 10 µM drug. After 30 s of incubation, the chase was started by delivery of buffer containing either 0, 2.5, 5, 7.5 or 10 µM drug concurrent with the start of data acquisition.

The smFRET data kinetic analysis. To construct cumulative distribution plots suitable for estimation of kinetic parameters, FRET traces were first idealized using hidden Markov model analysis to a model with three FRET states (FRET efficiencies, −0.0043 ± 0.06, 0.4485 ± 0.06 and 0.7070 ± 0.06) and then the cumulative sum of molecules that had arrived at the highest (0.7070) FRET state in each video frame was calculated. To estimate reaction mean times and their associated uncertainties, 1,000 bootstrap samples were generated from each experimental replicate and mean times were estimated by fitting of single-exponential functions to these data (equation (1)), taking into account unobserved events due to photobleaching of the fluorophores or dissociation of the intact ternary complex from the ribosomal A site by multiplying the estimated mean time with the inverse of the fraction of traces where accommodation was observed at the end of the process[25]:

$$f_{acc}(t) = \left(1 - e^{\frac{-1}{\frac{1}{f_{acc}(\infty)}\tau_{acc}}t}\right) \quad (1)$$

Mean rates and standard errors were calculated as the weighted averages of two to three experimental replicates for each drug concentration (f_{acc}, fraction of reactions reached the accommodation state; τ_{acc}, time required to reach the accommodation state). For estimation of drug residence times and rebinding

constants, these estimated mean times were plotted against drug concentration ([Drug]) and equation (2) was fitted to the data[25,26].

$$\tau_I([\text{Drug}]) = \tau_0\left(1 + \frac{[\text{Drug}]}{K_I}\right) \quad (2)$$

In equation (2), τ_I is the observed inhibition mean time as a function of drug concentration, τ_0 is the drug residence time each time it binds and K_I is the rebinding constant corresponding to the drug concentration required to double the inhibition time through drug rebinding events; it can be interpreted as the ratio between the drug association rate constant and the rate of the process that renders the ribosome immune to drug inhibition, in this case conformational changes in eEF1A.

Animal experiments. All animal experiments were approved by the University of California San Francisco Institutional Animal Care and Use Committee. Eμ-Myc/+ transgenic mice were purchased from the Jackson Laboratory (stock no. 002728). Primers used for genotyping were as follows: 5′-CCG AGG TGA GTG TGA GAG G-3′; 5′-AAA CAG TAA TAG CGC AGC A-3′. For Eμ-Myc clonal B-cell line collection, Eμ-Myc/+ mice harbouring lymphoma were euthanized according to Institutional Animal Care and Use Committee guidelines. Lymph nodes were collected immediately on ice, minced and passed through a 40 μm cell strainer in cold PBS with 2% FBS. Cells were centrifuged at 300*g* for 5 min. Cells were then resuspended in cold erythrocyte lysis solution ACK (Thermo Fisher A1049201) for 1 min. Isolated lymphoma cells were centrifuged at 300*g* for 5 min and washed in PBS before freezing in cell cryopreservation medium and storing in liquid nitrogen. For the lymphoma preclinical trial, Eμ-Myc/+ lymphoma cells were thawed and washed once in PBS. One million cells were injected intravenously into eight-week-old male C57BL/6 mice. Mice were monitored for lymphoma development by palpation every other day. Once the lymphoma tumours became palpable (approximately two weeks after tumour cell injection), mice (five per group) were dosed by intraperitoneal injection with either SR-A3 or vehicle (10% EtOH/Kolliphor EL in water) three times per week (every other day) until the survival end point (moribund mice were sacrificed; statistical significance of Kaplan–Meier survival curves was determined by logrank test) or for two weeks, at which time the tumours were dissected and weighed (statistical significance was determined by one-way ANOVA). The maximum allowable tumour size (2 cm in diameter) was not exceeded in any study. No animals or data points were excluded from the analyses.

Chemical synthesis (general). All reactions in non-aqueous media were conducted under a positive pressure of dry argon in glassware that had been dried in an oven prior to use, unless noted otherwise. Anhydrous solutions of reaction mixtures were transferred via an oven-dried syringe or cannula. All solvents were dried prior to use unless noted otherwise. Thin layer chromatography was performed using precoated silica gel plates (EMD Chemical; 60 g F254 plates). Flash column chromatography was performed on a CombiFlash Rf 200i system (Teledyne Isco). The ^{1}H and ^{13}C NMR spectra were obtained on a Varian Inova 400 MHz spectrometer recorded in parts per million (ppm; chemical shift, δ) downfield of TMS ($\delta = 0$) in $CDCl_3$ unless noted otherwise. NMR spectra were analysed using MestReNova v.14.1.1 (Mestrelab Research). Signal splitting patterns were described as singlet (s), doublet (d), triplet (t), quartet (q), quintet (quint) or multiplet (m), with coupling constants (*J*) in hertz. High-resolution mass spectra were obtained on a Waters Xevo G2-XS quadrupole time-of-flight liquid-chromatography/mass-spectrometry system, eluting with a water/MeCN (+0.1% formic acid) gradient at 0.6 ml min^{-1}. The Supplementary Information contains more details.

Statistics and reproducibility. The statistical significance of the difference between experimental groups was determined by one-way ANOVA, followed by Sidak's multiple comparisons test. *P* values indicate statistical significance denoted by $^{*}P < 0.05$, $^{**}P < 0.01$, $^{***}P < 0.005$ and $^{****}P < 0.0001$, and not significant by $P > 0.05$. Data were organized using Microsoft Excel 2017, and graphing and statistical analyses were performed using Prism 8.4.0. All biological experiments (except Fig. 6d) were repeated at least twice with similar results. The experiment in Fig. 6d was performed once with five mice allocated to each dose group. Descriptions of the error bars and the number of replicates within each experiment are provided in the figure legends.

Reporting summary. Further information on research design is available in the Nature Research Reporting Summary linked to this article.

Data availability

Data supporting the findings of this study are available within the Article and the Supplementary Information. Source data are provided with this paper.

References

37. Flis, J. et al. tRNA translocation by the eukaryotic 80S ribosome and the impact of GTP hydrolysis. *Cell Rep.* **25**, 2676–2688.e2677 (2018).
38. Blanchard, S. C., Kim, H. D., Gonzalez, R. L. Jr, Puglisi, J. D. & Chu, S. tRNA dynamics on the ribosome during translation. *Proc. Natl Acad. Sci. USA* **101**, 12893–12898 (2004).

Acknowledgements

Funding for this study was provided by the University of California San Francisco Program for Breakthrough Biomedical Research (J.T. and D.R.), the University of California San Francisco Invent Fund (J.T. and D.R.), the National Institutes of Health (5R01GM079238 to S.C.B. and R35CA242986 to D.R.), the American Cancer Society (American Cancer Society Research Professor Award to D.R.) and the Tobacco-Related Disease Research Program Postdoctoral Fellowship Awards (28FT-0014 to H.-Y.W.). Part of this work was supported by Taylor's University PhD Scholarship programme (A.A.Q.A.-K.), as well as a research grant from the Ministry of Education of Malaysia FRGS (600-IRMI/FRGS 5/3 (011/2017) to J.-F.F.W.).

Author contributions

H.-Y.W. and J.T. conceived the project, designed the experiments and analysed the data. H.-Y.W. synthesized, characterized and tested the compounds in the cellular experiments. H.-Y.W. and K.O. performed the OPP incorporation experiments. H.Y. and H.T. performed the mouse experiments. M.H. acquired and analysed the smFRET data. A.A.Q.A.-K. and J.-F.F.W. isolated the natural A3. D.R. and S.C.B. helped analyse data from the mouse lymphoma and smFRET experiments, respectively. H.-Y.W. and J.T. wrote the manuscript with input from all of the authors.

Competing interests

H.-Y.W., H.Y., K.O., D.R. and J.T. are listed as inventors on a patent application covering SR-A3 (PCT/US2021/016790, patent pending, University of California). S.C.B. holds equity interests in Lumidyne Technologies. D.R. is a shareholder of eFFECTOR Therapeutics, Inc., and is a member of its scientific advisory board. J.T. is a founder of Global Blood Therapeutics, Kezar Life Sciences, Cedilla Therapeutics and Terremoto Biosciences, and is a scientific advisor to Entos.

Additional information

Extended data is available for this paper at https://doi.org/10.1038/s41557-022-01039-3.

Supplementary information The online version contains supplementary material available at https://doi.org/10.1038/s41557-022-01039-3.

Correspondence and requests for materials should be addressed to Jack Taunton.

Peer review information *Nature Chemistry* thanks Mark Broenstrup, Youfu Luo and the other, anonymous, reviewer(s) for their contribution to the peer review of this work.

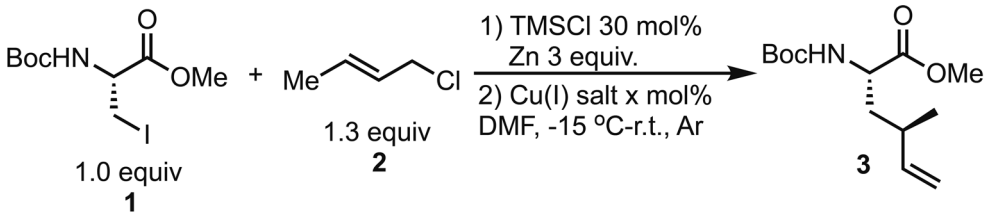

Entry	Cu(I) Salt	x	S_N2':S_N2 [a]	d.r. of S_N2' [a]	Yield [b]
1	CuBr·DMS	10	1.2:1	1:1	12%
2	CuBr·DMS	50	1.9:1	1.4:1	26%
3	CuBr·DMS	100	2.1:1	1.4:1	-
4	CuBr	100	1:3.5	-	-
5	CuCl	100	1:2.5	-	-
6	CuTC	100	-	-	N.R.
7[c]	CuBr·DMS	50	1:2.6	-	-
8[d]	**CuBr·DMS**	**50**	**1.8:1**	**1.4:1**	**43%**

[a] Ratio was based on the crude NMR of the reaction; [b] Isolated yield of **3**; [c] Crotyl bromide was used instead of **2**; [d] 2 equiv of crotyl chloride were used. DMS: dimethyl sulfide; TC: thiophene -2-carboxylate; N.R.: no reaction.

Extended Data Fig. 1 | Screening conditions for Cu(I)-promoted S_N2 reaction. The effect of various Cu(I) salts on the product ratios and yield was assessed.

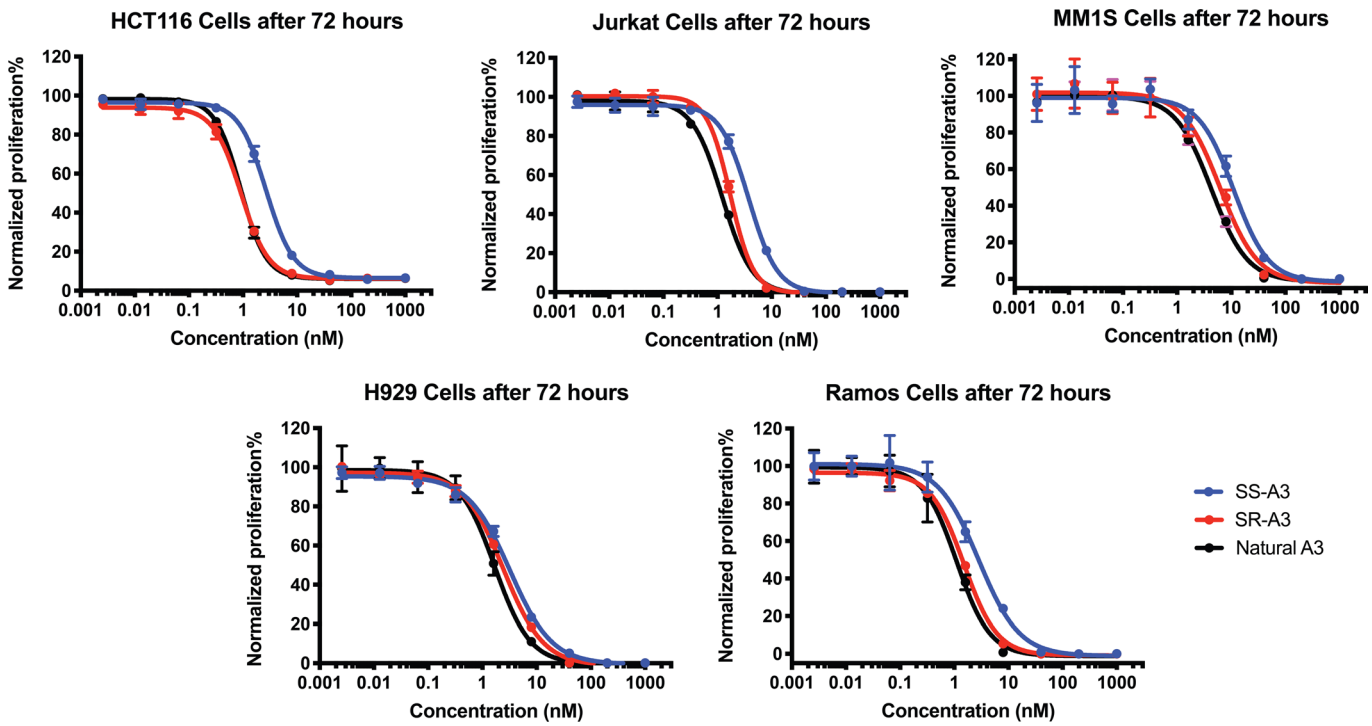

IC_{50} (nM)

	SS-A3	SR-A3	Natural A3
HCT116	2.67	0.92	0.91
Jurkat	3.78	1.71	1.22
MM1S	11.05	6.21	4.28
H929	3.20	2.43	1.69
Ramos	2.82	1.50	1.11

Extended Data Fig. 2 | Effects on cancer cell proliferation. The indicated cell lines were treated with DMSO or increasing concentrations of synthetic SR-A3 and SS-A3 and natural A3. After 72 h, cell proliferation was quantified using alamarBlue (% DMSO control, mean ± SD, n = 3). GraphPad Prism was used to calculate IC50 values.

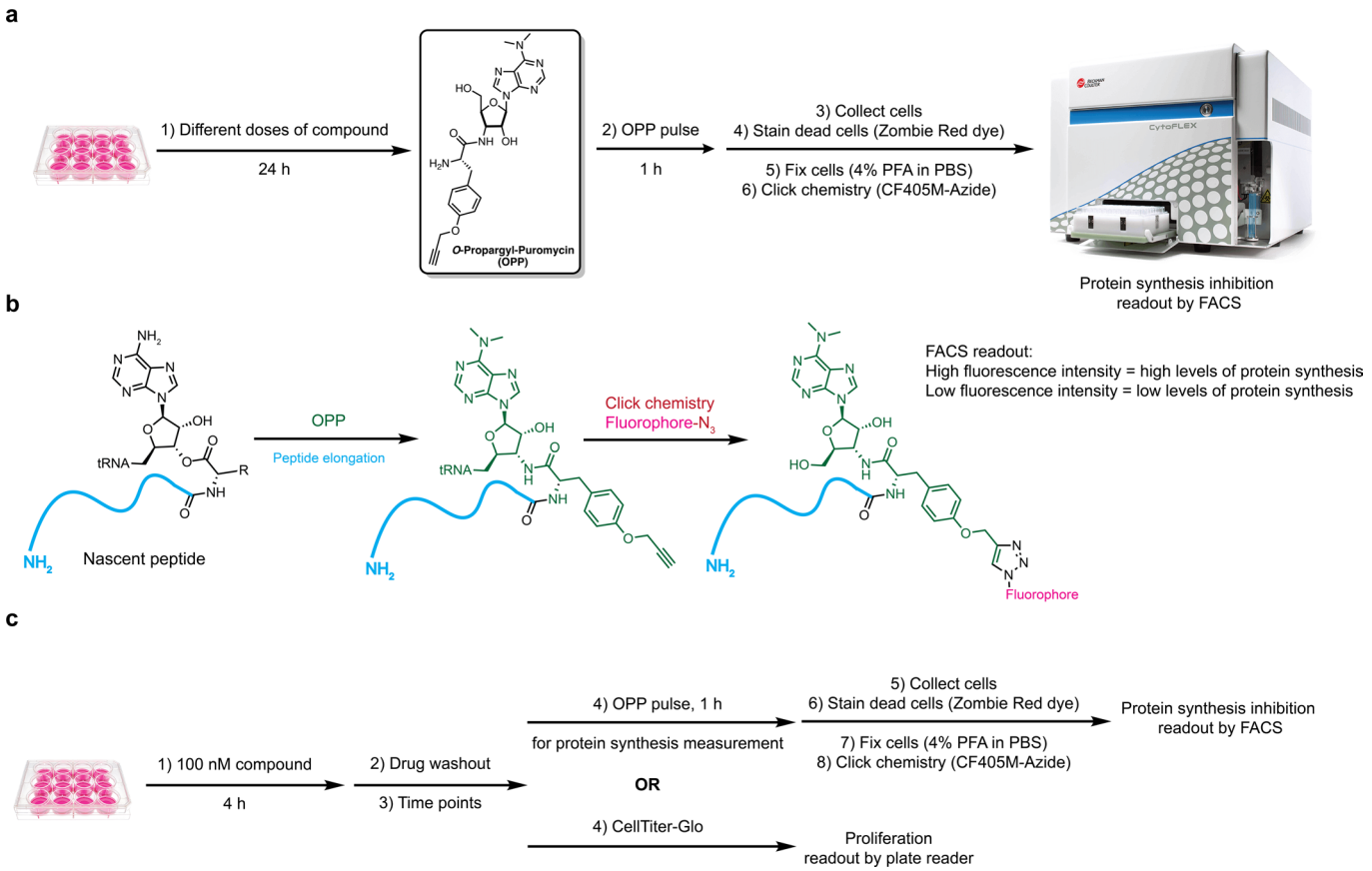

Extended Data Fig. 3 | Measuring effects on cellular protein synthesis rates. (**a**) General workflow for measuring protein synthesis rates in cells using *O*-Propargyl-Puromycin (OPP). See 'OPP incorporation assay' in the methods section for details. (**b**) OPP is an aminoacyl-tRNA mimic (clickable puromycin derivative) that, like puromycin itself, is incorporated into ribosome-associated nascent polypeptides by reacting with peptidyl-tRNAs in the ribosomal P site. After fixing and permeabilizing cells, click chemistry is used to conjugate the OPP alkyne with a fluorophore azide, and the intracellular fluorescence intensity (proportional to the amount of actively translating ribosomes) is measured by flow cytometry. (**c**) General workflow for washout-OPP and washout-proliferation experiments.

a

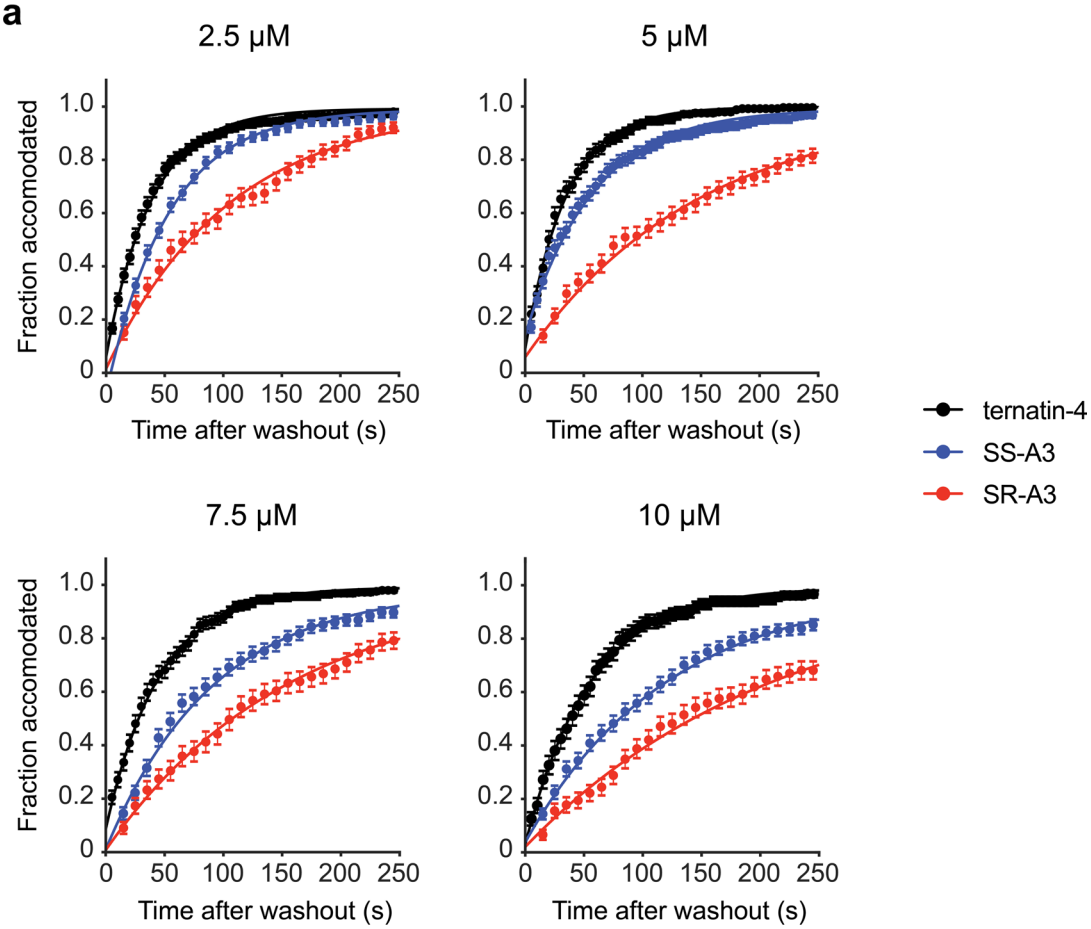

b

	Residence Time (s)	Inhibition Constant (μM)
ternatin-4	56 ± 4	10.4 ± 1.9
SS-A3	51 ± 2.5	5 ± 0.4
SR-A3	82 ± 1	2.67 ± 0.05

Extended Data Fig. 4 | Time and concentration-dependent effects on aa-tRNA accommodation revealed by smFRET. (**a**) Cumulative dissociation time distributions for ternatin-4, SS-A3, and SR-A3 at the indicated concentrations. Distributions are constructed as described in the main text and the methods. Error bars represent SEM derived from 1000 bootstrap replicates. (**b**) Tabulated kinetic parameters based on data in Fig. 5 and Extended Data Fig. 4a.

a

	Human Liver Microsome (remaining%)	Mouse Liver Microsome (remaining%)
ternatin-4	1.6%	1.2%
SS-A3	6.7%	7.4%
SR-A3	39.9%	31.8%

b

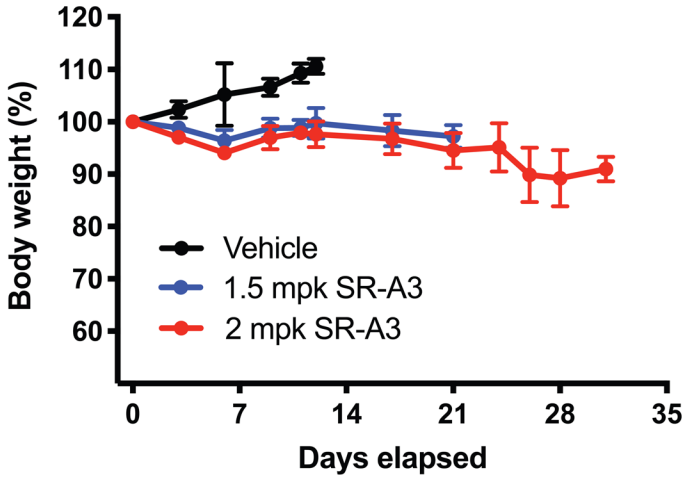

Extended Data Fig. 5 | Microsome stability and effects on mouse body weight. (**a**) Human and mouse liver microsome stability results. Percent remaining of each analog was quantified by LC/MS after incubating at 1 μM in the presence of human or mouse liver microsomes (with NADPH) for 30 min at 37 °C. This study was performed by the contract research organization, Bioduro-Sundia (San Diego, CA). (**b**) Average body weight (± SD, relative to day 0) during the efficacy study in Eμ-Myc mice (n = 5 per arm, Fig. 6a). Day 0 indicates the beginning of treatment.

a

	$t_{1/2}$ (h)	t_{max} (h)	C_{max} (ng/mL)	AUC_{Last} (h*ng/mL)	AUC_{Inf} (%)	AUC_{Extr} (%)	MRT_{Inf} (h)	AUC_{Inf}/D (h*kg*ng/mL/mg)
ternatin-4	5.16	0.250	51.3	151	186	19.4	6.17	92.8
SR-A3	8.21	0.583	86.6	347	384	9.78	8.63	192

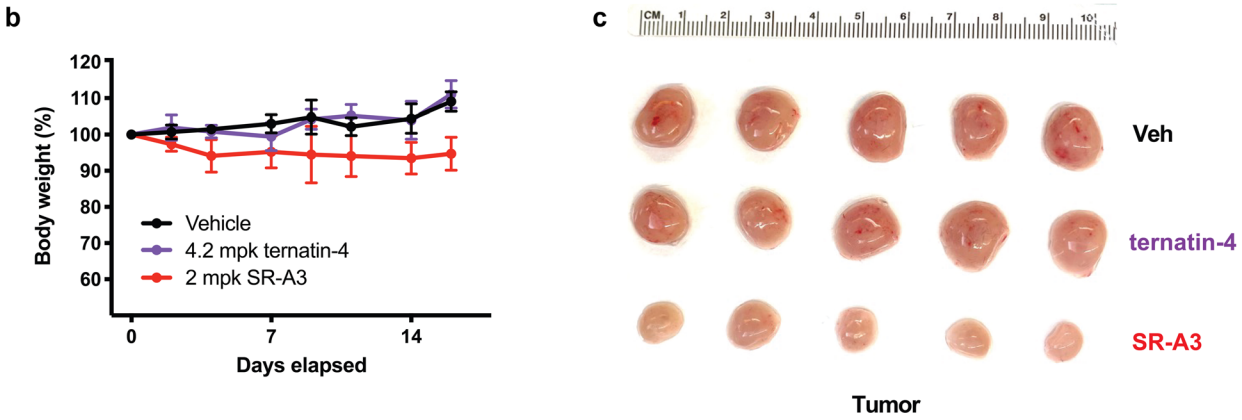

Extended Data Fig. 6 | Pharmacokinetics and effects of ternatin-4 and SR-A3 on mouse body weight and tumor size. (**a**) Mean pharmacokinetic (PK) parameters of ternatin-4 and SR-A3. Mice (n = 3) were intraperitoneally injected with ternatin-4 or SR-A3 (2 mg/kg), and plasma concentrations were quantified at various time points (Fig. 6b). PK data were acquired and analyzed by the contract research organization, Bioduro-Sundia (San Diego, CA). (**b**) Average mouse body weight (± SD, relative to day 0) during the Eμ-Myc tumor study (Fig. 6c). Day 0 indicates the beginning of treatment (n = 5 per arm). (**c**) Photographs of tumors from each mouse after two weeks of treatment (n = 5 per arm).

nature portfolio

Corresponding author(s): Jack Taunton

Last updated by author(s): Jul 17, 2022

Reporting Summary

Nature Portfolio wishes to improve the reproducibility of the work that we publish. This form provides structure for consistency and transparency in reporting. For further information on Nature Portfolio policies, see our Editorial Policies and the Editorial Policy Checklist.

Statistics

For all statistical analyses, confirm that the following items are present in the figure legend, table legend, main text, or Methods section.

n/a	Confirmed	
☐	☒	The exact sample size (*n*) for each experimental group/condition, given as a discrete number and unit of measurement
☐	☒	A statement on whether measurements were taken from distinct samples or whether the same sample was measured repeatedly
☐	☒	The statistical test(s) used AND whether they are one- or two-sided *Only common tests should be described solely by name; describe more complex techniques in the Methods section.*
☐	☒	A description of all covariates tested
☒	☐	A description of any assumptions or corrections, such as tests of normality and adjustment for multiple comparisons
☐	☒	A full description of the statistical parameters including central tendency (e.g. means) or other basic estimates (e.g. regression coefficient) AND variation (e.g. standard deviation) or associated estimates of uncertainty (e.g. confidence intervals)
☐	☒	For null hypothesis testing, the test statistic (e.g. *F*, *t*, *r*) with confidence intervals, effect sizes, degrees of freedom and *P* value noted *Give P values as exact values whenever suitable.*
☒	☐	For Bayesian analysis, information on the choice of priors and Markov chain Monte Carlo settings
☒	☐	For hierarchical and complex designs, identification of the appropriate level for tests and full reporting of outcomes
☒	☐	Estimates of effect sizes (e.g. Cohen's *d*, Pearson's *r*), indicating how they were calculated

Our web collection on statistics for biologists contains articles on many of the points above.

Software and code

Policy information about availability of computer code

Data collection	NMR data were collected on a 400 MHz (Varian) spectrometer. Fluorescence or luminescence intensity was measured on the SPARK plate reader (Tecan Austria GmbH). FACS data were collected on the CytoFLEX instrument (Beckman-Coulter). The time evolution of the FRET signal was recorded using a home-built total internal reflection-based fluorescence microscope at ~0.1 kW/cm2 laser (532 nm) illumination (Juette et al. Nat. Methods, 2016). Movies were recorded either in time-lapse mode with one 500 ms frame acquired every 10 seconds or continuously at a time resolution of 500 ms.
Data analysis	Statistical analyses and plots were generated using Graphpad Prism 8. NMR data were processed using MestReNova V14.1.1. Flow cytometry samples were analyzed using FlowJo V10.7.1. For smFRET experiments, donor and acceptor fluorescence intensities were extracted from the recorded movies and FRET efficiency traces were calculated using the SPARTAN software package (version 3.7.0, Juette et al. Nat. Methods, 2016). The resulting smFRET traces were analyzed using Hidden Markov model idealization methods as implemented in the SPARTAN software package.

For manuscripts utilizing custom algorithms or software that are central to the research but not yet described in published literature, software must be made available to editors and reviewers. We strongly encourage code deposition in a community repository (e.g. GitHub). See the Nature Portfolio guidelines for submitting code & software for further information.

Data

Policy information about availability of data

All manuscripts must include a data availability statement. This statement should provide the following information, where applicable:

- Accession codes, unique identifiers, or web links for publicly available datasets
- A description of any restrictions on data availability
- For clinical datasets or third party data, please ensure that the statement adheres to our policy

Data supporting the findings of this study are available within the article and the Supplementary Information. Source data are provided with this paper.

Field-specific reporting

Please select the one below that is the best fit for your research. If you are not sure, read the appropriate sections before making your selection.

☒ Life sciences ☐ Behavioural & social sciences ☐ Ecological, evolutionary & environmental sciences

For a reference copy of the document with all sections, see nature.com/documents/nr-reporting-summary-flat.pdf

Life sciences study design

All studies must disclose on these points even when the disclosure is negative.

Sample size	Sample size was determined based on our experimental observations and experience, in which a particular sample size was found to provide reliable and reproducible results.
Data exclusions	No data were excluded.
Replication	All biological data (except Fig. 6D) were replicated in at least two independent experiments. The experiment related to Fig. 6D was performed once, with 5 mice allocated to each dose group. Information on the number of replicates performed for each measurement is provided in the manuscript.
Randomization	For cell-based assays, cells were randomly allocated into each experimental group. Mice from the studies related to Figure 6 were randomized to groups based on body weights.
Blinding	For cell-based experiments, blinding is not relevant as our samples were treated uniformly, and the same data analysis procedure was applied to all samples of the same experiment. In the mouse survival study (Fig. 6A), a vet who was blinded to the group allocation was responsible for determining the endpoint of each mouse. In the mouse tumor weight study (Fig. 6D), blinding is not relevant since individual tumors were harvested, processed, and weighed in parallel using identical procedures.

Reporting for specific materials, systems and methods

We require information from authors about some types of materials, experimental systems and methods used in many studies. Here, indicate whether each material, system or method listed is relevant to your study. If you are not sure if a list item applies to your research, read the appropriate section before selecting a response.

Materials & experimental systems

n/a	Involved in the study
☒	☐ Antibodies
☐	☒ Eukaryotic cell lines
☒	☐ Palaeontology and archaeology
☐	☒ Animals and other organisms
☒	☐ Human research participants
☒	☐ Clinical data
☒	☐ Dual use research of concern

Methods

n/a	Involved in the study
☒	☐ ChIP-seq
☐	☒ Flow cytometry
☒	☐ MRI-based neuroimaging

Eukaryotic cell lines

Policy information about cell lines

Cell line source(s)	HCT116, H929, MM1S, Jurkat, Ramos, and HEK293T cells were purchased from American Type Culture Collection (ATCC). Mutant HCT116 cells (HCT116-417) were obtained from Dr. Dominic Hoepfner (Krastel et al., Angew. Chem. Int. Ed., 2015).
Authentication	No additional authentication was performed.

Mycoplasma contamination	All the cell lines were routinely tested and were negative for mycoplasma.
Commonly misidentified lines (See ICLAC register)	No commonly misidentified cell lines were used.

Animals and other organisms

Policy information about studies involving animals; ARRIVE guidelines recommended for reporting animal research

Laboratory animals	The Eμ-Myc/+ transgenic mice (male, 7-9 weeks old) were purchased from the Jackson Laboratory (stock no. 002728). Male C57BL/6 mice, 7-9 weeks old, weighing 15-25 grams. Animals were housed in a pathogen-free barrier environment, at ~20 °C on a 12/12-h dark/light cycle throughout the study, and were supplied water ad libitum. All experiments were performed in compliance with guidelines approved by the Institutional Animal Care and Use Committee of UCSF under approval no. AN180952-02B.
Wild animals	This study didn't involve wild animals.
Field-collected samples	This study didn't involve samples collected from the field.
Ethics oversight	All animal experiments were approved by The University of California San Francisco Institutional Animal Care and Use Committee (UCSF-IACUC, approval no. AN180952-02B).

Note that full information on the approval of the study protocol must also be provided in the manuscript.

Flow Cytometry

Plots

Confirm that:

☒ The axis labels state the marker and fluorochrome used (e.g. CD4-FITC).

☒ The axis scales are clearly visible. Include numbers along axes only for bottom left plot of group (a 'group' is an analysis of identical markers).

☒ All plots are contour plots with outliers or pseudocolor plots.

☒ A numerical value for number of cells or percentage (with statistics) is provided.

Methodology

Sample preparation	HCT116 cells at 60% confluency in 12-well plates were incubated with the indicated concentrations of ternatin analogs for 10 min or 24 h at 37°C. After the indicated times, O-propargyl-puromycin (30 μM final concentration) was added, and the cells were incubated for 1 hour at 37°C. Subsequently, media was removed, and the cells were trypsinized, collected, and washed twice with ice-cold PBS before transferring to a 96-well V bottom plate. 100 μL Zombie Green (BioLegend, San Diego, CA) solution was added to each well and incubated for 30 min at RT in the dark. Cells were then washed with 2% FBS in PBS before fixation 139 with 200 μL of 4% PFA in PBS for 15 min on ice in the dark. After washing the cells with 2% FBS in PBS, 200 μL permeabilization buffer (3% FBS, 0.1% saponin in PBS) was added to each well, and the cells were incubated for 5 min at RT in the dark. Cells were then washed and resuspended in 25 μL permeabilization buffer. 100 μL click chemistry mix (50 mM HEPES pH 7.5, 150 mM NaCl, 400 μM TCEP, 250 μM TBTA, 5 μM CF647-Azide (Biotium, Fremont, CA), 200 μM CuSO4) was added to each well, and cells were incubated at RT in the dark. After overnight incubation, the cells were washed with permeabilization buffer followed by FACS buffer (2% FBS, 1% P/S, 2 mM EDTA, in PBS w/o Ca/Mg). Cells were then resuspended in 200 μL FACS buffer and filtered before FACS analysis.
Instrument	CytoFLEX (Beckman-Coulter)
Software	Flow cytometry samples were analyzed using FlowJo V10.7.1.
Cell population abundance	A total of 20,000 events was collected in each condition; After gating for single live cells, an average of 15,000 cells were analyzed (represents 75% of the total events). FSC and SSC parameters were used to determine single cells from all collected events.
Gating strategy	1. FSC vs. SSC to determine cells. 2. FSC-H vs. FSC-A to determine single cells. 3. FITC-H vs. FSC-H to determine live cells.

☒ Tick this box to confirm that a figure exemplifying the gating strategy is provided in the Supplementary Information.